Dynamic Response of CubeSat Structures Under Launch Loads: Effects of Internal Mass Distribution

Prajwal Hiremath
M.Sc. Candidate in Space Engineering, Technische Universität Berlin
Berlin, Germany
prajwal.v.hiremath0@gmail.com, prajwal.hiremath@campus.tu-berlin.de

***Abstract*—During launch, CubeSats are subjected to severe loads, and the internal mass distribution within their structures can significantly affect their dynamic response and overall structural behavior. An investigation of the structural and dynamic behavior of a CubeSat in representative launch environments, with particular emphasis on internal mass distribution, is crucial to the design and development of a CubeSat structure. A finite element model of the CubeSat is developed using a simplified but realistic structural representation, including deployer-representative boundary conditions and internal subsystem masses arranged in several alternative configurations. Quasi-static analysis is performed first using equivalent inertial load cases to assess stress distribution, displacement, and structural load transfer. Then modal analysis was performed to identify the fundamental natural frequencies and dominant mode shapes for each configuration. Finally, a random vibration analysis is performed with power spectral density inputs from a selected launcher to study the acceleration response. By comparing multiple internal mass layouts, the study examines how mass placement alters modal characteristics, modifies load paths, and affects the overall structural behavior of the CubeSat during launch. The results are used to identify trends relevant to the early-stage CubeSat design, particularly with respect to structural robustness and the protection of sensitive subsystems. The proposed approach provides a practical framework for structural assessment and offers design-oriented insight to improve the launch survivability of small satellite platforms.**

***Index Terms*—CubeSat, structural dynamics, random vibration, static analysis, finite element analysis, mass distribution, mode shapes, fundamental natural frequency**

I. Introduction

CubeSats are one of the most significant innovations in modern space engineering. Since their introduction more than two decades ago, they have now become an important class of small satellites. Features such as short development cycles, a standardized form factor, and low development costs have enabled a wide range of applications, from hands-on space education to commercial, governmental, and scientific missions. CubeSats are modular units [U] of $10\,\mathrm{cm} \times 10\,\mathrm{cm} \times 10\,\mathrm{cm}$, with common configurations such as 1U, 3U, 6U, and 12U. Standardization simplifies integration with deployment systems, enabling frequent access to outer space.

With such small-scale dimensions, a CubeSat contains tightly packed subsystems, and it has to withstand intense dynamic loads during launch. The structural integrity and survivability of sensitive onboard components depend on the structures' response to quasi-static accelerations, broadband random vibrations, and high-frequency shock events. Hence, the mechanical design of a CubeSat structure and the placement of its internal subsystems play a key role in mission success. In general, CubeSats are stored in a standardized dispenser system for the entire duration of launch until deployment, restricting movement, and protecting the satellite throughout the launch phases. The interface between these two independent systems is critical, as they define the boundary condition and stiffness, which directly influence the overall dynamic behavior of the structure [1], [2].

Most CubeSat structural research revolves around the verification of a specific configuration to survive harsh launch conditions using finite element analysis, random vibration qualification, modal behavior testing, stress distribution and structural response under representative launch conditions, thus reinforcing the importance of structural dynamics in small satellite design [3], [4]. Due to their compact form factor, design is often governed by packaging constraints rather than ideal structural placement. Hence, it is equally important to assess how the internal mass distribution influences the structure of a CubeSat in the early stages of the design. The mass distribution alters the dynamic loads that reach the sensitive components, the stiffness-to-mass characteristics, which affect the natural frequencies, the mode shapes, and the load paths. With changes in the placement of structural components, keeping the total mass the same has inertial effects, often resulting in greater flexibility, amplified deformations in certain modes, and a change in natural frequencies. The effects are evident when components such as batteries or payloads are clustered or placed away from primary load paths, highlighting the need to consider mass distribution early to achieve structurally efficient and launch-resilient designs.

This paper investigates the dynamic response of a simplified 3U CubeSat under representative launch loads, focusing on the internal mass distribution. A finite element model with deployer-representative boundary conditions is used to perform quasi-static, modal and random vibration analyses, evaluating stress, displacement responses, modes and response of the structure to random vibration. The aim is to understand how the mass distribution influences structural behavior and to identify trends that support more robust early-stage design decisions for a CubeSat mission.

II. CubeSat Structural Model

For this work, a 3U rail-type CubeSat structural model is developed, according to the Cal Poly design specification [5]. CubeSats are widely available in 1U, 3U, 6U and 12U configurations. The 3U configuration is one of the most widely adopted designs, offering an effective compromise between available internal volume, structural simplicity, and compatibility with standardized rail-based deployment systems [6], [7]. It provides sufficient flexibility for arranging the internal subsystem masses and payload elements, making it suitable for investigating how different mass layouts influence stiffness, inertia properties, and dynamic response. The spacecraft envelope is taken as per [5], [8] as $100 \times 100 \times 340.5$ mm, with the CubeSat coordinate system defined at the geometric center of the structure. The baseline CubeSat configuration is designed to be symmetric about its principal axes, providing a simplified structural model that facilitates a clear understanding of the dynamic response of the system under applied loading conditions.

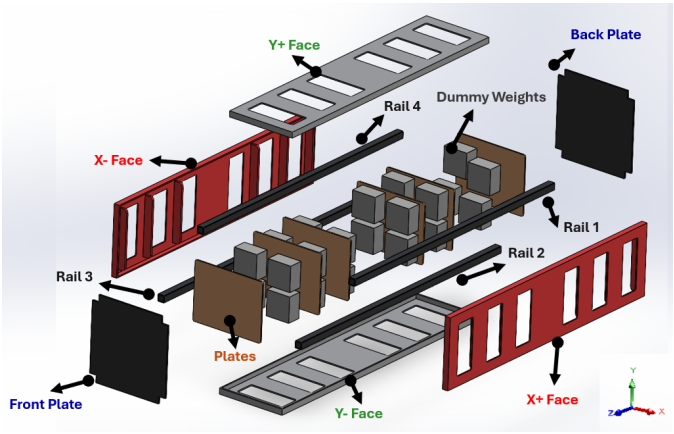


Fig. 1: Exploded view of the designed 3U CubeSat.

Figure 1 presents an exploded view of the 3U CubeSat structural model developed for this study. The primary structure consists of four longitudinal rails, external side panels, upper and lower end plates, and a series of internal support plates intended to accommodate representative subsystem masses. These masses are idealized as discrete elements, each with a mass of 125 grams, and are arranged on the internal plates to enable the investigation of various mass distribution configurations. The internal plates are supported by features that are directly integrated into the side panels, providing a simplified and continuous load transfer path through the primary load-bearing structure. This modeling strategy improves the interpretability of load transmission within the structure and is particularly advantageous for evaluating the effect of internal mass distribution on the global structural response. In line with the specification, the rail regions are treated as critical dispenser-contact features, with all geometric constraints, tolerances, and interface requirements defined according to the CubeSat Design Specification and associated interface control guidelines [5], [9].

The total mass of a typical 3U CubeSat is generally in the range of 4–6 kg [5], [6]. In the present study, a total mass of approximately 4 kg is achieved, which remains within the lower bound of the standard 3U mass envelope. The primary structural configuration, consisting of rails, external face plates, and internal load-bearing plates, has a mass of 1002.2 g. To represent internal subsystems, 24 discrete lumped masses of 125 g each are introduced, resulting in a total system mass of 4002.2 g (~ 4 kg).

The primary structure is modeled using Aluminium 7075-T651, which is widely used in CubeSat structures due to its high strength-to-weight ratio and favorable mechanical properties. The material properties considered for this material are highlighted in Table I. This material selection is consistent with the standard practices and recommendations outlined in the CubeSat design guidelines, where Aluminium alloys (particularly 7075 variants) are commonly adopted for structural components and rail interfaces to ensure compatibility with deployer systems [5], [7]. The total mass is maintained constant across all configurations, while the internal mass distribution is varied systematically between cases. This approach enables a focused investigation of the influence of center-of-gravity shifts and inertia distribution on the structural response and dynamic behavior of the CubeSat under launch loading conditions.

TABLE I: Material properties of 7075-T651

Property	Value	Unit
Elastic Modulus	7.17×10^{10}	N/m^2
Poisson's Ratio	0.33	–
Shear Modulus	2.69×10^{10}	N/m^2
Mass Density	2810	kg/m^3
Tensile Strength	5.72×10^{8}	N/m^2
Yield Strength	5.03×10^{8}	N/m^2
Thermal Expansion Coefficient	2.36×10^{-5}	K^{-1}
Thermal Conductivity	130	W/(m·K)
Specific Heat	960	J/(kg·K)
Damping Ratio	0.001	–

A. Internal Mass Distribution Cases

To examine the influence of internal mass distribution on the structural and dynamic behaviour of the CubeSat, a series of mass configuration cases is defined. In accordance with the CubeSat design guidelines [5], the permissible CoG displacement is constrained to ± 20 mm in the X and Y directions and ± 70 mm in the Z direction. First, a symmetric baseline configuration is established in which the center of gravity (CoG) coincides with the geometric center of the structure. Figure 2 shows the baseline configuration, where the internal masses are symmetrically distributed such that the center of gravity (CoG) coincides with the geometric center of the structure at $(0, 0, 0)$.

Subsequently, additional cases, as shown in Figure 3 are generated by redistributing the internal masses to introduce controlled CoG offsets along the principal axes. For each axis, two offset magnitudes within the admissible range are considered, along with a combined lateral case to represent a more

realistic, non-uniform mass distribution. The configurations are defined by their nominal offsets, with realized CoG locations listed in Table II, enabling a systematic evaluation of their effect on the structural response under representative launch loads.

TABLE II: CoG locations for Mass Cases

Case	Description	CoG (X, Y, Z) [mm]
Case 0	Baseline	(0, 0, 0)
Case 1	X +10 mm	(10, 0, 0)
Case 2	X +20 mm	(20, 0, 0)
Case 3	Y +10 mm	(0, 10, 0)
Case 4	Y +20 mm	(0, 20, 0)
Case 5	Z +35 mm	$(0, 0, \sim 35)$
Case 6	Z +70 mm	$(0, 0, \sim 70)$
Case 7	X + Y (combined)	$(\sim 15.5, \sim 15.5, 0)$

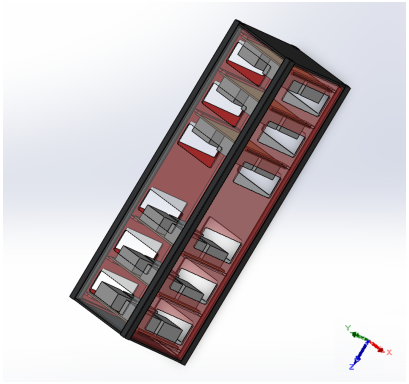
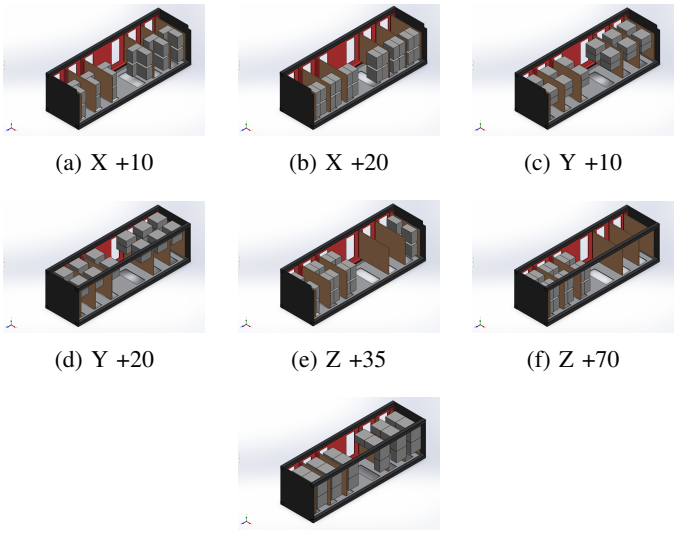


Fig. 2: Baseline Configuration



(a) X +10 (b) X +20 (c) Y +10

(d) Y +20 (e) Z +35 (f) Z +70

(g) X + Y

Fig. 3: Configurations illustrating the applied COG offsets

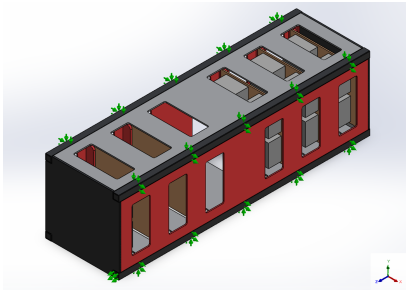


Fig. 4: Boundary Condition

III. Finite Element Modelling, Boundary Conditions, and Loading Definition

The finite element model is developed to represent the CubeSat structure under realistic launch conditions, with boundary conditions applied to approximate a typical deployer interface through rail constraints. The boundary conditions applied are shown in Figure 4. Since the primary load transfer between the CubeSat and the deployer occurs through the rail interfaces, these regions are constrained to replicate the mechanical support provided during launch. Accordingly, the faces aligned with the X and Y directions are constrained to restrict lateral motion, representing confinement within the deployer rails. In the axial (Z) direction, only one rail interface face is constrained to limit displacement, while the remaining faces are left unconstrained to avoid over-constraining the model and to better represent the realistic retention and release conditions within the deployer. These boundary conditions capture the mechanical interaction between the CubeSat and the deployer during launch.

To define the loading environment, the Falcon 9 launch vehicle is selected, as it is one of the most widely used platforms for CubeSat missions and provides a representative and well-documented set of launch loads [10]. Based on Falcon 9 payload integration guidelines, the CubeSat is assumed to be oriented such that its longitudinal axis (Z-axis) is perpendicular to the rocket flight direction, consistent with standard deployer configurations. The quasi-static loading is defined using limit load factors for payloads below 1000 kg, including axial accelerations ranging from $-6g$ to $+11g$ and lateral accelerations up to $\pm 7.5g$, applied along the main axes as shown in Figure 5. In addition, the dynamic environment is represented through a qualification power spectral density (PSD) profile over the frequency range of 20–2000 Hz as shown in Figure 7 and Figure 6, ensuring that the structural response captures both static and vibration-induced effects associated with launch.

A. Analysis Mesh Properties

The finite element mesh was generated in SolidWorks simulation ® using a blended curvature-based meshing approach to accurately capture geometric features and stress gradients. The resulting mesh provided a good balance between accuracy and computational efficiency. Table III lists the mesh parameters applied in the analysis tool.

A mesh sensitivity study was conducted to ensure convergence in all analyses. For quasi-static analysis, a finer mesh with a maximum element size of 1 mm was adopted to

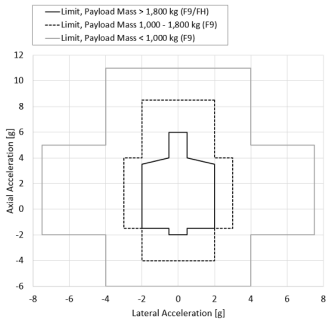


Fig. 5: Falcon 9 Limit Load Factors

Frequency	Falcon 9/Falcon Heavy payload Random Vibration MPE (P95/50) (g^2/Hz), All axes
20	0.0044
100	0.0044
300	0.01
700	0.01
800	0.03
925	0.03
2000	0.00644
GRMS	5.13

Fig. 6: Falcon 9/Falcon Heavy random vibration qualification levels

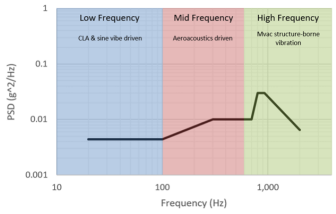


Fig. 7: Falcon 9/Heavy Random Vibration MPE

TABLE III: Mesh parameters for different analyses

Parameter	Static	Modal	Random Vibration
Meshing Approach	Blended Curvature-Based Mesh		
Max. Element Size	1 mm	1.5 mm	4 mm
Min. Element Size	0.05 mm	0.075 mm	0.20 mm
Min. Elements in a Circle	8		
Element Growth Ratio	1.4		
Mesh Density	Fine Mesh		

accurately resolve stress distributions. In the modal analysis, a maximum element size of 1.5 mm was selected, providing a good balance between accuracy and computational efficiency while ensuring convergence of the natural frequencies. For random vibration analysis, a coarser mesh with a maximum element size of 4 mm was used to reduce computational time, while still maintaining sufficient accuracy in the dynamic response.

IV. Quasi-Static Analysis

During launch, a satellite is subjected to rapidly varying load conditions resulting from vibration, shock, and inertial effects associated with acceleration. The challenge is due to these different types of load acting at the same instant, and representing these as a function of frequency and time is highly complex. Hence, they are idealized by an equivalent quasi-static load that reproduces the same maximum stress or strain response. Under conservative and worst-case loading conditions, this becomes an effective and efficient methodology to evaluate a spacecraft's structural integrity. Within this dynamic environment, the payload experiences axial accelerations induced by engine thrust and aerodynamic drag, as well as lateral accelerations originating from wind gusts, engine gimbaling, stage separation events, and other transient perturbations.

A. Static Load Case

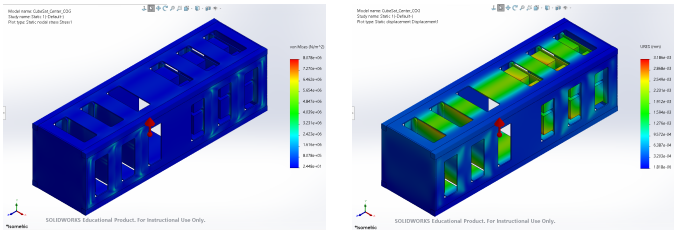
The quasi-static analysis characterizes the worst-case structural response, hence only the most critical loading condition is examined rather than investigating the complete spectrum of limit load factors. The maximum axial acceleration of $+11g$ is applied along the principal axis, representing the most severe launch loading scenario. This strategy yields a conservative estimate of the structural response while reducing computational cost and is adequate for a comparative assessment of the influence of different internal mass distribution configurations.

B. Static Structural Response

Table IV presents a synthesis of the quasi-static analysis results for the different configurations of the mass distribution, reporting, for each case, the maximum von mises stress together with the corresponding displacement.

TABLE IV: Quasi-static analysis results for different CoG configurations

CoG	Von Mises Stress (MPa)	Max Displ. (mm)
Center	8.078	3.186×10^{-3}
X(10,0,0)	12.83	4.908×10^{-3}
X(20,0,0)	12.61	5.740×10^{-3}
Y(0,10,0)	19.92	8.759×10^{-3}
Y(0,20,0)	32.15	1.534×10^{-2}
$Z(0, 0, \sim 35)$	25.94	1.431×10^{-2}
$Z(0, 0, \sim 70)$	25.68	1.486×10^{-2}
$XY(\sim 15.5, \sim 15.5, 0)$	1.858	2.305×10^{-3}

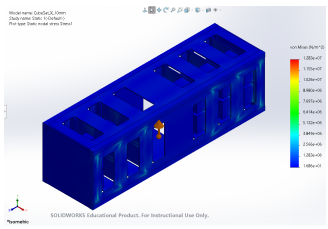


(a) Center Case Stress (b) Center Case Displacement

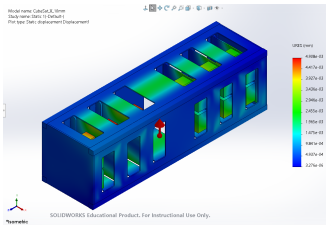
Fig. 8: Quasi-static response for CoG at Center (0,0,0).

V. Modal Analysis

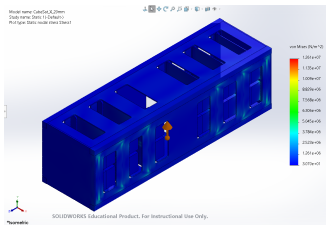
Modal analysis is conducted to determine the natural frequencies and corresponding mode shapes of the CubeSat structure based solely on its mass and stiffness distribution



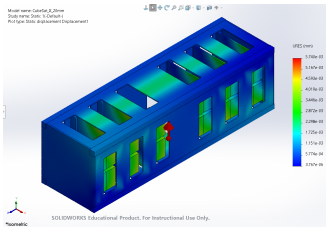
(a) X Case (10,0,0) Stress



(b) X Case (10,0,0) Displacement

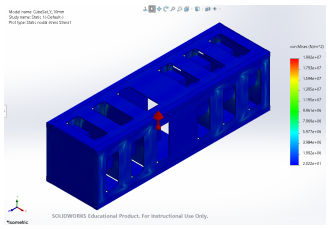


(c) X Case (20,0,0) Stress

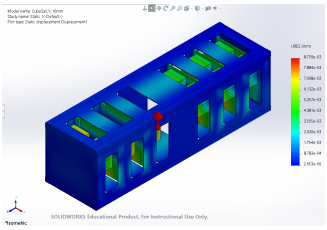


(d) X Case (20,0,0) Displacement

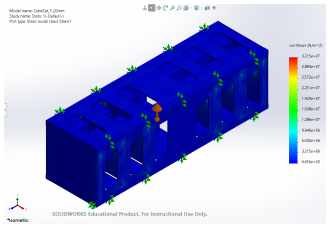
Fig. 9: Quasi-static response for X-direction CoG offsets.



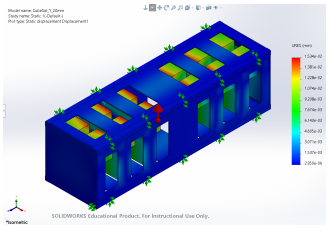
(a) Y Case (0,10,0) Stress



(b) Y Case (0,10,0) Displacement



(c) Y Case (0,20,0) Stress



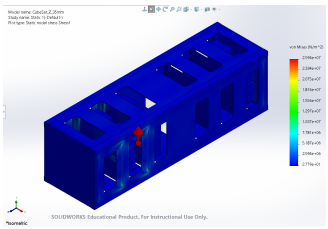
(d) Y Case (0,20,0) Displacement

Fig. 10: Quasi-static response for Y-direction CoG offsets.

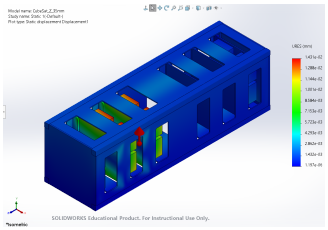
under the applied boundary conditions. No external loads are applied in this analysis, as the inherent dynamic characteristics are obtained by solving the eigenvalue problem of the system. The first five natural frequencies are extracted that represent the dominant structural responses and are most relevant for assessing potential resonance with the launch vehicle environment. This approach provides an efficient, yet sufficiently accurate basis for comparing the influence of different internal mass distribution configurations.

A. Modal analysis results for different CoG configurations

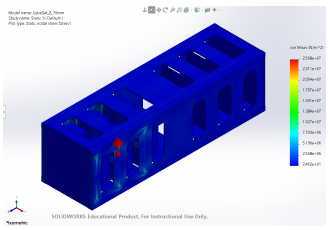
The modal response of the CubeSat structure is shown in Figure 13, along with the first five natural frequencies for each CoG configuration, summarized in Table V. From the results, it is observed that the first mode shape remains



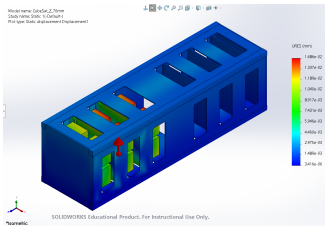
(a) Z Case (0,0,35) Stress



(b) Z Case (0,0,35) Displacement

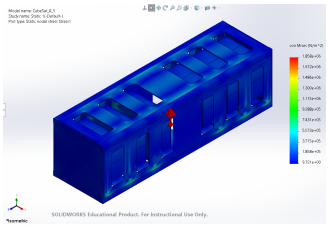


(c) Z Case (0,0,70) Stress

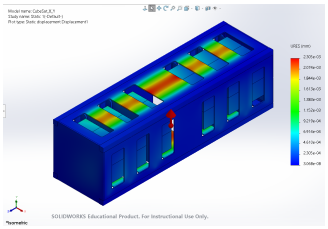


(d) Z Case (0,0,70) Displacement

Fig. 11: Quasi-static response for Z-direction CoG offsets.



(a) XY Case Stress



(b) XY Case Displacement

Fig. 12: Quasi-static response for XY (15,15,0) offsets.

predominantly consistent across most CoG configurations, exhibiting a global bending behavior of the structure, except the cases X20 and XY with opposite behavior compared to other cases, suggesting that the fundamental dynamic response is largely governed by the overall structural layout. However, the natural frequencies show a strong dependence on the location of CoG. A significant reduction of up to 132 Hz is observed for configurations Z35 and Z70, which involve mass shifts toward the Z-axis compared to 212.78 Hz for the baseline case, thus indicating a reduction in global stiffness. In contrast, the cases X10, X20, Y10 and Y20 show moderate reductions in frequency values ranging approximately between 166 Hz and 181 Hz. While the overall deformation pattern remains similar, slight localized deformation effects are observed in cases with larger offsets, particularly in the X20 configuration, highlighting the influence of asymmetric mass distribution. The combined XY configuration exhibits significantly higher natural frequencies, indicating a redistribution of stiffness and mass that alters the dominant deformation behavior. Overall, the results demonstrate that the dynamic response of the structure is highly sensitive to the placement of the internal mass, with the longitudinal offsets (Z-axis) having the most pronounced effect.

Note: It is observed that the second, third, and fourth modes exhibit closely spaced natural frequencies. This behavior is attributed to the geometric symmetry of the structure, resulting in similar stiffness characteristics along multiple directions and leading to near-degenerate modal responses.

TABLE V: Results (Hz) for different CoG configurations

Mode	COG	X10	X20	Y10	Y20	Z35	Z70	XY
1	212.78	216.37	176.93	180.47	166.73	132.97	132.64	606.46
2	220.53	224.57	179.21	184.40	170.35	133.89	133.60	1185.9
3	220.55	224.60	179.25	184.41	170.36	283.25	170.31	1279.9
4	220.58	224.63	179.39	184.49	170.38	291.33	478.54	1281.4
5	284.77	281.20	226.89	229.50	203.56	488.22	507.75	1289.1

In Figure 13 and Figure 14, the deformation is scaled for visualization purposes and does not represent actual displacement magnitudes.

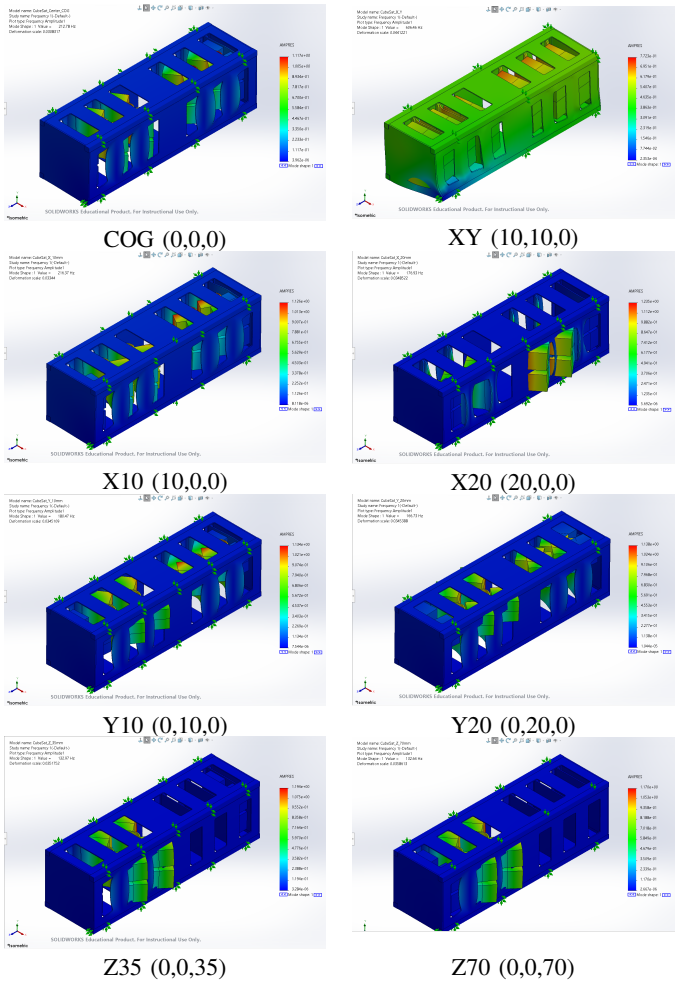


Fig. 13: Comparison of first mode shapes for different CoG

Furthermore, the shapes of the second mode for all configurations are compared in Figure 14, which exhibits greater sensitivity to mass distribution compared to the fundamental mode, showing variations in deformation patterns in all configurations. The baseline and small-offset cases maintain a largely global deformation behavior, however larger X20 and Z configurations show increased localization of deformation. The reduction in values for the Z cases indicates a decrease in the effective structural stiffness. As the natural frequency of a system is proportional to the square root of the stiffness-to-mass ratio, a more flexible structural response leads to lower frequencies, whereas configurations with higher effective stiffness exhibit correspondingly higher natural frequencies. However, the XY configuration exhibits significantly higher frequency and a comparatively stiffer response. These observations indicate that higher-order modes are more influenced by the asymmetric mass distribution and local structural flexibility.

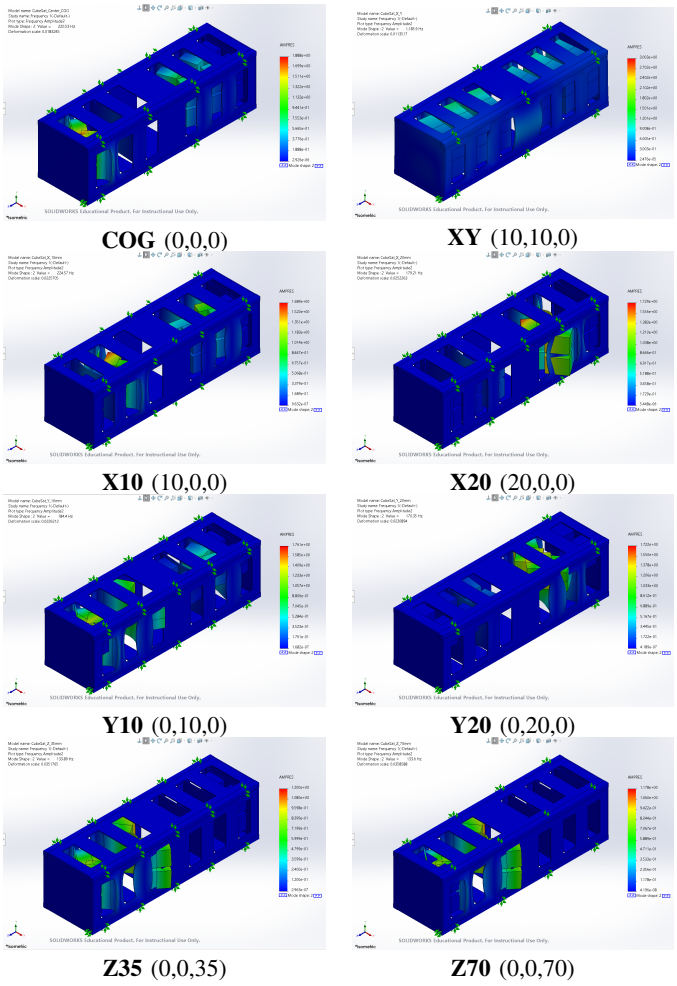


Fig. 14: Comparison of second mode shapes for different CoG

VI. Random Vibration Analysis

Random vibration typically arises from engine vibrations and acoustic loads, which consist of a wide spectrum of frequencies with amplitudes varying randomly during launch. These are most severe for a small satellite and its deployers, as a random vibration time history cannot be expressed in a simple mathematical form. To solve this, statistical methods are used to describe it. The most common method is the Root Mean Square (RMS) acceleration, where G_{rms} represents the standard deviation of the acceleration signal for a zero-mean

vibration history. Since vibration energy is distributed over different frequency ranges, the overall G_{rms} is divided into smaller frequency bandwidths for analysis. Within each bandwidth, the G_{rms} value is calculated, squared, and normalized by the bandwidth to yield the power spectral density (PSD), expressed in G^2/Hz. PSD plots are then used to visualize how vibration energy is distributed across frequencies, providing valuable information on which frequency ranges dominate the vibration environment. This frequency-domain representation is essential for predicting structural response, identifying potential resonances, and ensuring the satellite design can withstand launch loads without damage. In this study, as the SpaceX Falcon 9 PSD is applied as the input excitation at the CubeSat deployer interface, the response is evaluated at a node located at the end and corner of the CubeSat rail, as this area constitutes the main load transfer interface between the satellite and the operator during launch. The rails are the sole structural components in direct contact with the deployer and therefore undergo the largest transmission of vibration and acceleration loads. Choosing a node at the rail corner tip ensures that the recorded response reflects the worst-case dynamic amplification imparted to the structure. Moreover, this location is affected by both global bending modes and local deformation phenomena, making it a robust indicator of the overall structural behavior under random vibration. Using the same extraction point for all mass distribution configurations, it is possible to perform a direct and meaningful comparison of how internal mass placement influences the dynamic response. A modal damping ratio of $\zeta = 0.03$ is used for random vibration analysis. This lies within the 1–5% range reported for small aerospace assemblies [11], [12]. Space standards commonly assume 5% for spectral methods (SRS, $Q = 10$) [13], and CubeSat studies adopt 5% as a conservative default for random vibration and shock response simulations [14]. Experimental modal tests of bolted metallic structures show damping governed by joint friction, typically in the few-percent range [15]. Hence, the value of 0.03 was considered for analysis conservatively.

A. Structural Response with Effect of Mass Distribution

1) X-axis: The random vibration response on the X-axis is presented in Figure 15. From the results, it is evident that the dominant frequency band is around 600-900 Hz, with most configurations showing peaks in this band, particularly in the Z35 and Z70 cases. These cases have reduced stiffness in the X-direction when the mass is shifted along the Z direction, showcasing strong coupling with bending modes. The baseline case with CoG at (0,0,0) is more stable and follows the expected structural response without excessive amplification. The lateral offset cases, namely, X10, X20, Y10, and Y20 show moderate amplification compared to baseline, and Z35 and Z70 show a more distributed response across frequencies. The XY case is different from the rest as it shows a completely broader response and fewer peak-dominated points, has a lower maximum amplification, and represents a more realistic but less critical dynamic condition.

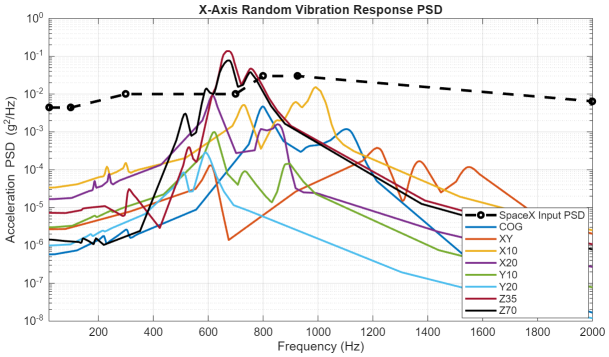


Fig. 15: Response in the X-axis for different CoG

2) Y-axis: The random vibration response on the Y-axis is presented in Figure 16. It can be inferred that the dominant frequency band is 500–900 Hz. The baseline configuration has a smooth and controlled response, with no extreme peaks compared to offset cases. Additionally, almost all configurations show strong peaks in this range. Peaks indicate major dynamic amplification, likely from higher-order modes and structural coupling. The Z35 and Z70 cases show a very strong low-frequency amplification, which occurs early at around 500–650 Hz, due to reduced stiffness and strong excitation of global bending behavior. However, for the Z cases, the response drops significantly. The X10 and X20 cases show significant peaks around 700–900 Hz, suggesting strong coupling between lateral mass asymmetry and Y-direction loading. The Y cases show reduced peak amplitudes across the frequency band. Mass shifts along Y may stabilize the response compared to the Z and X cases. The XY case has no sharp dominant peak, energy is spread across frequencies, thus representing a less critical and more realistic case.

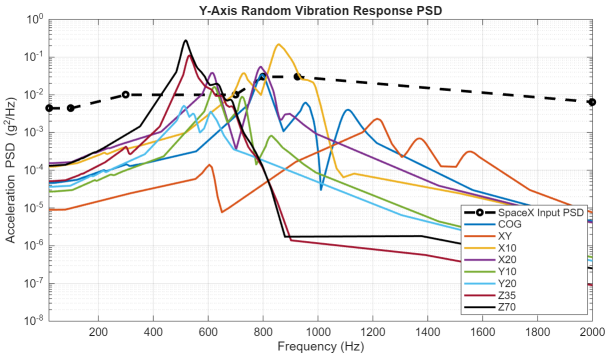


Fig. 16: Response in the Y-axis for different CoG

3) Z-axis: The random vibration response on the Z-axis is presented in Figure 17. The most dominant response is observed in this study in all cases. With the dominant amplification in the range of 600–900Hz. The response for all cases is higher than for the X and Y cases. The baseline case shows the largest amplification, thus highlighting that the baseline is not always the lowest response case under the Z-axis excitation. Similarly, the X10, X20, Y10 and XY peaks are similar to the

baseline case, suggesting that the lateral mass redistribution can still strongly affect the axial/random vibration response. The Z35 and Z70 cases do not produce the largest peaks, with a smoother response after the main amplification region, suggesting that axial mass offsets may reduce participation in some Z-axis response modes. The Y20, is the only case with much lower response compared to other cases. So, for Z-axis excitation, the COG case shows the highest peak, while the Y20 and Z-offset cases give comparatively more controlled responses.

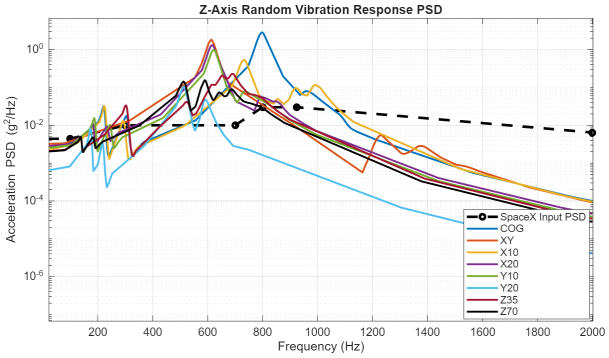


Fig. 17: Response in the Z-axis for different CoG

VII. Conclusion

The analysis shows that the internal mass distribution has a significant influence on the structural and dynamic response of the CubeSat under launch conditions. From the quasi-static analysis, it can be seen that the Y20 case experiences the highest stress of about 32.15 MPa, with a very small displacement recorded of 0.01534 mm. The resulting stresses are well below the material yield strength, and hence no risk of permanent deformation under the specified loading condition. The analysis confirms the adequate structural integrity.

Modal analysis indicates that the first mode remains largely consistent across the tested configurations. However, the natural frequencies are sensitive to the mass placements, as it is evident that the mass shifts across the Z-axis led to a noticeable reduction in fundamental frequency, showcasing reduced stiffness, whereas lateral offsets cause moderate variations. Higher modes exhibit greater sensitivity, with more localized deformation patterns in asymmetric cases.

For random vibrations, the response is dominated by amplification in the 500–900 Hz range, driven by higher-order modes and structural coupling. The X-axis is influenced by Z-offset cases, while the Y-axis exhibits the most pronounced variation across mass distribution cases due to its role as the primary launch direction. The Z-axis shows the highest amplification levels, mainly influenced by localized dynamic effects. Compared with the SpaceX input PSD, local exceedance near resonance is observed and is consistent with expected dynamic amplification, whereas near-nominal mass distributions provide a more controlled response.

In general, the study confirms that maintaining the CoG close to (0,0,0) leads to a more balanced and predictable structural response. However, the results indicate that the optimal mass distribution remains case dependent and all configurations should be evaluated with respect to the specific loading conditions and design requirements. For future work, the analysis can be improved by adopting more refined and controlled meshing strategies beyond the default SolidWorks settings ®and incorporating detailed subsystem models, realistic joints, or interface behavior to provide a closer representation of actual flight conditions, as well as by performing experimental validation through physical tests, such as random vibration or modal testing of a representative structure.

Acknowledgment

The author acknowledges the support of Technische Universität Berlin and all individuals who contributed through technical discussions and academic guidance.

References

[1] S. D. Bury, R. McMurran, D. Pignatelli *et al.*, "Analysis and mitigation of the cubesat dynamic environment," in *Proceedings of the 33rd Annual AIAA/USU Conference on Small Satellites*, 2019, accessed: 2026-03-17. [Online]. Available: https://s3vi.ndc.nasa.gov/ssri-kb/static/resources/19160715.pdf

[2] L. Araújo, "Dynamic response of a cubesat within a deployer during the launch environment," https://fenix.tecnico.ulisboa.pt/downloadFile/1126295043841614/Extended-Abstract_Leticia-Araujo_91600.pdf, 2024, extended abstract, accessed: 2026-03-17.

[3] A. Elshaal *et al.*, "Structural analysis of alainsat-1 cubesat," *Ain Shams Engineering Journal*, 2024, accessed: 2026-03-17. [Online]. Available: https://www.sciencedirect.com/science/article/pii/S1110982324000528

[4] V. Bostan *et al.*, "Structural analysis and vibration testing of a cubesat microsatellite," *Journal of Engineering Science*, 2024, accessed: 2026-03-17. [Online]. Available: https://repository.utm.md/bitstream/handle/5014/31210/JES-4-2024_8-21.pdf?isAllowed=y&sequence=1

[5] Cal Poly CubeSat Program, "Cubesat design specification (1u–12u), rev. 14.1," Feb. 2022, accessed: 2026-04-19. [Online]. Available: https://www.cubesat.org/cubesatinfo

[6] NASA CubeSat Launch Initiative, "Cubesat 101: Basic concepts and processes for first-time cubesat developers," https://www.nasa.gov/wp-content/uploads/2017/03/nasa_csli_cubesat_101_508.pdf, 2017, accessed: 2026-03-17.

[7] The CubeSat Program, "Poly picosatellite orbital deployer mk. iii rev. e user guide," 2014, accessed: 2026-04-19. [Online]. Available: https://www.cubesat.org/cubesatinfo

[8] Cal Poly CubeSat Program, "Cubesat specification drawings, rev. 14," 2020, accessed: 2026-04-19. [Online]. Available: https://www.cubesat.org/cubesatinfo

[9] Cal Poly CubeSat Laboratory, "Cubesat inspection and fit-check procedure (cifp)," 2020, accessed: 2026-04-19. [Online]. Available: https://www.cubesat.org/cubesatinfo

[10] SpaceX, "Falcon 9 payload user's guide," https://www.spacex.com/assets/media/falcon-users-guide-2025-05-09.pdf, May 2025, accessed: 2026-04-23.

[11] SOLIDWORKS Help, "Viscous damping ratios for different systems and materials," 2026.

[12] K. Okuyama, K. Yoshikawa, and C. Oue, "A simple method for identifying the natural frequency of a micro satellite with a primary structure made of aluminum alloy," *Aerospace*, vol. 11, p. 436, 2024.

[13] National Aeronautics and Space Administration, "Pyroshock test criteria," NASA, Washington, DC, Tech. Rep. NASA-STD-7003A, 2011.

[14] C. J. Eriksson, "Finite element analysis of stresses in the mist cubesat due to dynamic loads during launch," Master's thesis, KTH Royal Institute of Technology, Stockholm, Sweden, 2021.

[15] W. Xu, "Effect of bolted joint preload on structural damping," Master's thesis, University of South Florida, Tampa, FL, 2013.